Pergamon

Int. J. Heat Mass Transfer. Vol. 39, No. 9, pp. 1827–1838, 1996

0017-9310/96 $15.00+0.00

0017-9310(95)00276-6

Advanced micro-fin tubes for evaporation

L. M. CHAMRA and R. L. WEBB†
Department of Mechanical Engineering, Penn State University, University Park, PA 16802, U.S.A.

and

M. R. RANDLETT
Olin Brass Corp., Cuba, MO 65453, U.S.A.

(*Received* 27 *December* 1994 *and in final form* 21 *July* 1995)

Abstract—R-22 evaporation data are presented for new micro-fin geometries applied to the inner surface of 15.88 mm outside diameter tubes. The purpose of the work was to develop internal geometries having higher evaporation coefficients than existing single-groove micro-fin designs. The new geometries include both single-helix and cross-grooved surfaces. The single-groove geometries have 74–80 internal fins, 0.35 mm fin height, and 30° fin included angle. The cross-groove geometries are formed by applying a second set of grooves at the same helix angle, but opposite angular direction as the first set. Data are provided for varying second groove depths. Data are reported for evaporation at 2.2°C in a 2.44 m long test section for 45–181 kg h^{-1} mass flow rate. The series 1 tests are for inlet and exit qualities of 0.20 and 0.80, respectively. The evaporation coefficient reaches a maximum at 20° helix angle and then decreases for higher helix angle. The highest performance was provided by a cross-grooved tube having 20° helix angle. Its evaporation coefficient is 23% higher than an existing 75 groove, single-helix tube. The pressure drop is 6% higher than in the 75 groove tube. Reduced performance occurs in the cross-grooved tube when the second groove depth exceeds 60% of the depth of the first set of grooves. The series 2 data stimulate complete evaporation with exit superheat in circuit lengths of 7.3, 9.8 and 12.2 m. These data clearly show that the evaporation coefficient attains a maximum as the average vapor quality in the 2.44 m test section approaches 90%. The vapor quality at which the maximum occurs decreases with increasing flow rate or heat flux.

INTRODUCTION

A special 'enhanced' copper tube commonly called the 'micro-fin tube' has found major success in residential air conditioners and is described by Webb [1]. This tube, illustrated in Fig. 1, has small fins of triangular cross section at a helix angle of approximately 8–30° (measured from the tube center line). Refrigerant is either evaporated or condensed in the tube. A significant fraction of new air cooled residential air conditioners use this tube. This includes central air conditioners and window units. The tube was first developed by Fujie *et al.* [2] of Hitachi Cable Ltd and is described by Tatsumi *et al.* [3]. An improved Hitachi design is described by Shinohara and Tobe [4] and by Shinohara *et al.* [5]. The version described by Shinohara and Tobe [4] is close to that now made by tube manufacturers in Japan, Europe and the U.S.A. The tube is made in diameters of 6.35, 7.94, 9.5, or 14.3 and 15.9 mm. The micro-fin tube provides enhancement of 100% or more for both condensation or evaporation.

Numerous papers have been published that report the performance of micro-fin tubes. Among these are Eckels *et al.* [6], who provided R-22 evaporation coefficients and pressure drop at 2.0°C for five currently used micro-fin tube geometries. The reported evaporation coefficient is the average value for 0.10 entering and 0.85 leaving vapor quality. Schlager *et al.* [7] tested three 12.7 mm outside diameter micro-fin tubes having different helix angles (15, 18 and 25°) with R-22. However, their tubes also had different fin heights ($0.15 \leqslant e_i \leqslant 0.3$ mm) and pitches, and they did not define the effect of specific geometry factors on the performance differences. Their test results for all three geometries agree very closely. Thors and Bogart [8] report data on the Wolverine 9.0 mm outside diameter, 60 groove tube for R-22 evaporation. Morita *et al.* [9] report data on 4.0 and 6.0 mm outside diameter tubes. These investigators do not report the effect of heat flux, which is known to exist and was reported by Chiang [10]. Chiang tested four micro-fin tubes with different axial and helical grooves using R-22 as the working fluid. He reported that the evaporation heat transfer coefficient increases with heat flux for both helical and axial grooved tubes. Schlager *et al.* [11, 12], Eckels and Pate [13], Chiang [10] and Ha and Bergles [14] report the effect of oil on the

† Author to whom correspondence should be addressed.

NOMENCLATURE

A	heat transfer surface area, $A_o = \pi D_o L$, $A_i = \pi(D_o - 2t_w)L$ [m^2]
C	a constant in equation (4)
C_1, C_2	constants in equation (6)
D_i	tube inside diameter, or diameter to the base of internal fins or roughness [mm]
D_o	tube outside diameter [mm]
e	primary groove fin height [mm]
G	mass velocity [kg m^{-2} s^{-1}]
h	heat transfer coefficient [W m^{-2} K^{-1}]
k	thermal conductivity [W m^{-1} K^{-1}]
L	tube length [m]
$\dot{m}$	mass flow rate [kg s^{-1}]
n	exponent for equation (4) and equation (6)
p	axial pitch of surface or roughness elements [mm]
Pr	Prandtl number
Q	heat rate [W]
q''	heat flux [W m^{-2}]
Re	Reynolds number, $\rho u D/\mu$
R_w	wall thermal resistance [K W^{-1}]
t_w	tube minimum wall thickness [m]
T	temperature: T_w (water), T_{sat} (saturation) [°C]
u	liquid velocity [m s^{-1}]
U	overall heat transfer coefficient [W m^{-2} K^{-1}]
x	local vapor quality.

Greek symbols

α	helix angle relative to tube axis [deg]
β	fin included angle [deg]
η	efficiency index, $(h/h_p)/(\Delta p/\Delta p_p)$
ΔT_{lm}	log mean temperature difference [K]
Δp	pressure drop [kPa]
Δx	change in vapor quality
μ	viscosity [N s m^{-2}]
ρ	density [kg m^{-3}].

Subscripts

i	designates inner surface of tube
in	inlet of the test section
h	hydraulic
out	outlet of the test section
o	designates outer surface of the tube
p	plain tube
sat	saturation
t	total
w	water.

performance. Oil slightly reduces the evaporation coefficient for typically used oil concentrations.

Yoshida *et al.* [15] performed a detailed experimental study, in which they measured local R-22 evaporation coefficients on the top, side and bottom of the tube for a range of vapor qualities and mass velocities. They conclude that the narrow grooves carry liquid to the sides and top of the tube by capillary wetting. Thus, thin films are provided around the entire tube circumference. Low heat transfer coefficients exist on the top and sides of the plain tube at low mass velocity, because the tube surface is dry.

The key objective of the present work was to develop higher performance micro-groove geometries for evaporation. This paper presents data on advanced single-helix, and cross-grooved geometries developed for evaporation. The performance is compared with that of an existing typical commercial geometry reported by Thors and Bogart [8].

METHOD OF MANUFACTURE

The micro-fin geometry and the tube were made using an innovative manufacturing method. This involves embossing a flat strip, which is passed through a set of rollers, one of which is embossed with the desired micro-groove geometry. Then, the tube is rolled into a circular shape and the axial seam is induction welded. This manufacturing process is able to make higher fins (0.35 mm), and fins having a smaller included angle (30°), than currently produced using seamless tube. The tube is made with 0.58 mm fin pitch. A single helix micro-fin geometry made in the preferred manner will have greater internal surface area, which contributes to the higher performance. A second innovative cross-groove geometry was also manufactured. These "cross-grooved" tubes are made by forming a primary set of grooves [Fig. 1(b)], and then forming a second set of grooves, which cross the first set. The resulting geometry is shown in Fig. 1(b′). The second set of grooves may be equal to, or less than the first set of grooves. The cross-grooved tubes provide increased surface area, relative to the single-helix design, and provide higher performance.

TEST SECTION GEOMETRIES

Table 1 lists the tube geometries and provides a code for reference to each geometry tested (or compared). The MX™ and MCG™ geometries were manufactured by Olin Brass Corp. Each of the MX™ and MCG™ geometries were made with helix angles (α) of 15, 17.5, 20 and 27°. These geometries are described by a code. For example, MX™-20 indicates

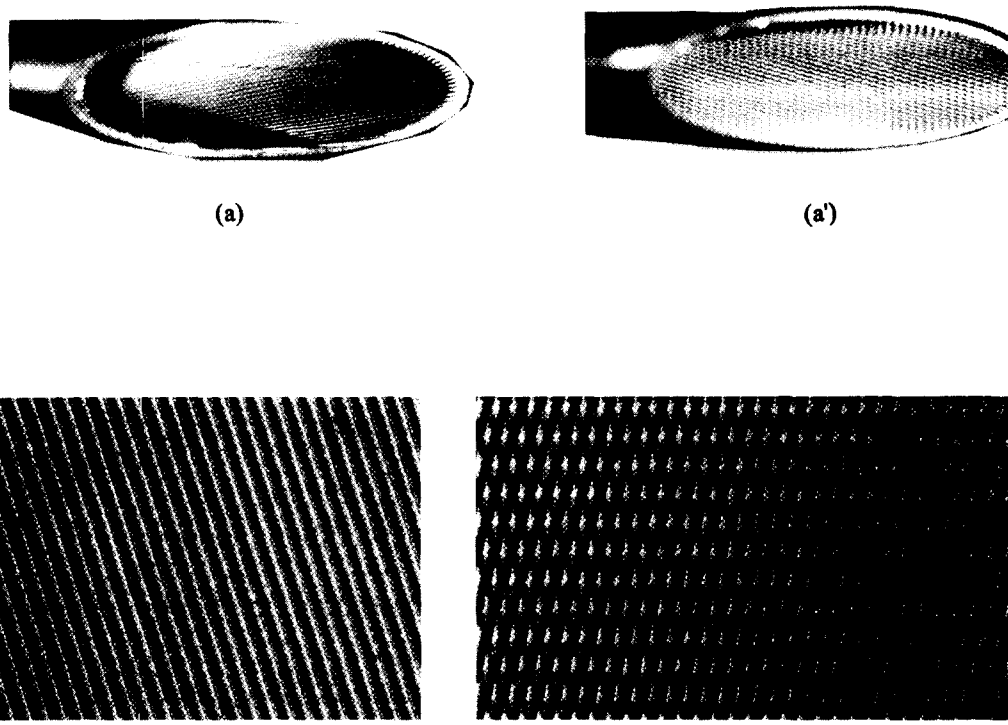

Fig. 1. (a) MX™ micro-fin tube, (b) plain view of MX™ tube, (a′) MCG™ micro-fin tube, (b′) plain view of MCG™ tube.

a micro-fin tube with single helix geometry having a 20° helix angle, and MCG™-27 indicates a micro-fin tube with cross-grooves (MCG™) geometry having a 27° helix angle. The MX™ and MCG™ tubes are shown in Fig. 1. Table 1 also lists the DX™-60 and DX™-75 geometries, manufactured by Wolverine Tube Inc. and reported by Thors and Bogart [8]. These tubes are included as a comparison base, and our data are compared with the DX™-60 and DX™-75 data reported by Thors and Bogart [8] which were taken in a similar apparatus at similar condition.

The single-helix tubes are in the MX™ series, and the DX™-60 and DX™-75 tubes. The micro-fin shape of the MX™ series tube is different from that of the DX™ tubes. The key differences are: (1) fin height is 0.35 mm vs 0.30 mm for the DX™ tubes, (2) a fin included angle of 30° vs 40° for the DX™ tubes. Further, the MX™ series tubes have 74–80 internal

Table 1. Micro-fin tubes

	MX™ helix	MCG™	DX™-60	DX™-75
Geometry type	Helical	Cross groove	Helical	Helical
D_o [mm]	15.88	15.88	15.88	15.88
D_i [mm]	14.88	14.88	14.87	14.87
Number of fins	74 at $\alpha = 27°$ 78 at $\alpha = 20°$ 76 at $\alpha = 17.5°$ 74 at $\alpha = 15°$	74 at $\alpha = 27°$ 78 at $\alpha = 20°$ 76 at $\alpha = 17.5°$ 74 at $\alpha = 15°$	60	75
Fin height, e [mm] (2nd entry = depth of the second groove set)	0.35	0.35/0.21* 0.35/0.17 0.35/0.14*	0.30	0.30
Fin pitch, p [mm]	0.58	0.58	0.76	0.622
Helix angle, α [deg]	15, 17.5, 20, 27	15, 17.5, 20, 27	27	23
Fin included angle, β [deg]	30	30	40	40
e/D_i	0.024	0.024	0.020	0.020
p/e	1.66	1.66	2.53	2.04

* These tubes made only with 17.5° helix angle except for 0.35/0.07 which is also made with 27° helix.

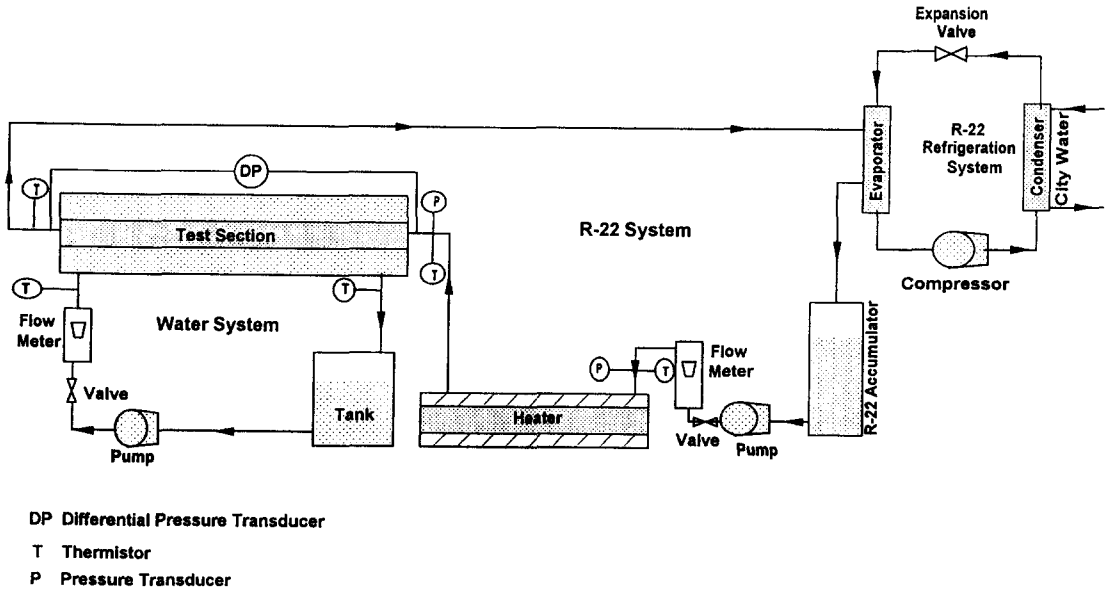

Fig. 2. Schematic drawing of the test facility.

fins, as opposed to 60 and 75 for the DX™-60 and DX™-75 tubes, respectively. All of these differences should promote increased internal surface area per unit length.

The MCG™ tubes have a "cross-groove" pattern. The first set of grooves in the MCG™ tubes are identical to those in the MX™ tubes. However, a second set of grooves is applied to form the cross-groove geometry. The second set of grooves is applied at the same helix angle, but opposite angular direction as the first set. As shown in Table 1, one series of the MCG™ tubes (15, 17.5, 20 and 27°) were made with a groove depth 50% that of the first groove (0.17 mm). A second set of MCG™ tubes was also made using 17.5% helix angle, in which the depth of the second set of grooves were made at 40%, 50%, 60% and 80% depth of the first groove set. Using the coding scheme, a tube having 17.5° helix angle with the second groove set having 50% the depth of the first set is described as MCG™-17.5 @ 50%.

TEST APPARATUS

Figure 2 is a schematic drawing of the apparatus used for in-tube vaporization and condensation tests. The test rig consists of three closed loops: (1) the test section R-22 loop, (2) a water loop and (3) an R-22 heat rejection loop. The instrumentation includes an on-line data acquisition system driven by a personal computer, which is used to measure thermistor and pressure transducer outputs.

The test section refrigerant loop consists of the test section, a condenser, a variable speed pump, a flow meter and a pre-heater. A detailed schematic of the test section is shown in Fig. 3. The 2.44 m (8 ft) long test section is a counter flow, double tube heat-exchanger with water flowing in an annulus and R-22 evaporating inside the circular tube. The annulus exists between 22.22 and 15.88 mm outside diameter tubes. The refrigerant inlet and exit temperatures are measured using a thermistor at each location. The error in temperature measurements is ± 0.1°C. In addition, a pressure transducer measures the test section inlet pressure.

The refrigerant (R-22) exits the test section and goes to a shell-and-tube condenser. The R-22 condenses on the shell side against lower pressure R-22 evaporating on the tube side. The liquid refrigerant is circulated in the test section loop by a gear pump, which is located between the condenser and the pre-heater. The gear pump has a capacity of 0.05 l min^{-1} (50 gal h^{-1}) and is magnetically coupled to the drive motor. A calibrated, variable area flow meter located between the gear pump and the pre-heater measures R-22 flow rates up to 0.044 l min^{-1} (42 gal h^{-1}). The flow meter is accurate within 1% of full scale.

The vapor quality entering the test section is controlled by a horizontal 12 kW, electric pre-heater. The power to the pre-heater is controlled by a chopped cycle controller and the power input is measured by a 3-phase watt-hr meter. A thermistor and a pressure transducer, located at the pre-heater inlet, establish the thermodynamic state of the liquid entering the pre-heater. This measurement, along with the electric energy supplied in the pre-heater, are used to determine the R-22 vapor quality entering the test section.

The water loop consists of the test section annulus, a centrifugal pump, a magnetic flow meter, and a water tank containing an electric heater. The hot water flows in the annulus and evaporates the test section refrigerant. The water enters and leaves the test section from the bottom and top of the annulus in order to insure a uniform distribution of hot (cold) water around the inner tube. The inlet and exit water tem-

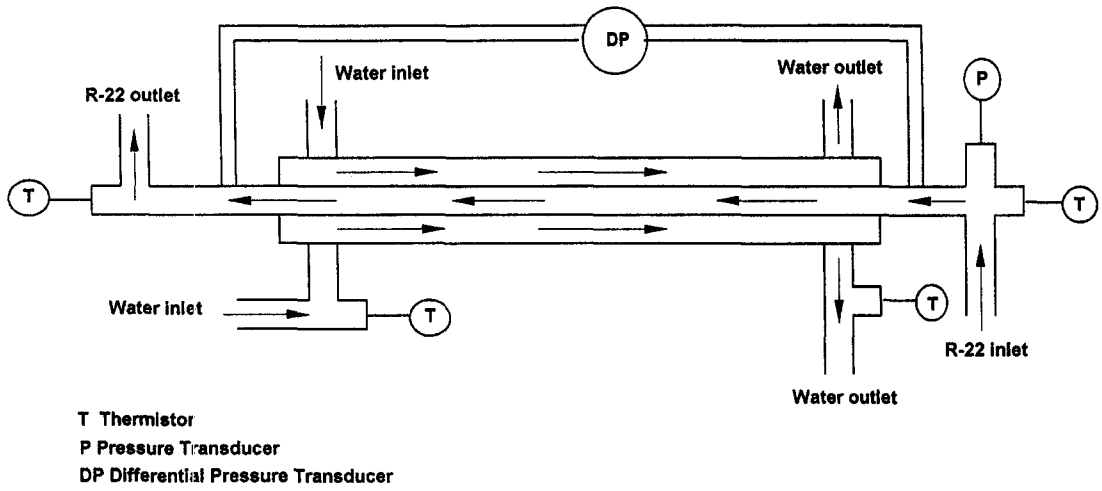

Fig. 3. A detailed schematic of the test section.

peratures are measured by a pair of thermistors. The water returns to the water tank where it is pumped through the test section by a centrifugal pump. The water flow rates are measured using a magnetic flow meter. The flow rate is controlled by a valve located after the centrifugal pump.

The R-22 heat rejection loop condenses the refrigerant evaporated on the tube side of the test section. This R-22 loop contains a variable speed, 3 h.p. motor driving a reciprocating compressor. The compressor speed is governed by an adjustable frequency controller. An automatic controller is used to set the evaporation temperature, which is affected by controlling the compressor speed.

TEST PROCEDURE AND DATA REDUCTION

Data are normally taken for incomplete evaporation in a test section 2.44–3.66 m long. Two methods have been used to obtain the data. We will describe these as the "h vs $\dot{m}$" method, and the "constant heat flux" methods. These methods are described below.

h *vs* ṁ *method*

Many of the previously referenced investigations have taken data for fixed inlet and fixed exit vapor quality in the test section. An example of this is the data of Thors and Bogart [8]. Their data are taken in a 15.88 mm o.d., 3.66 m long test section for 10% and 80% entering and leaving vapor qualities, respectively. Their data are plotted as h vs mass flow rate ($\dot{m}$). A disadvantage of this method is that the heat flux is not constant on the h vs $\dot{m}$ plot. The heat flux is proportional to the mass flow rate in such a test. Hence, as the mass flow rate increases, so does the heat flux.

Constant heat flux method

Chamra and Webb [16] and Ha and Bergles [14] have shown that the heat transfer coefficient is sensitive to heat flux. One may separate the mass velocity and heat flux dependency by taking data to show the variation of the local heat transfer coefficient as a function of mass velocity (G) for fixed heat flux. For constant heat flux in a fixed tube diameter, $\Delta x \propto G$. Hence, as G increases (for constant heat flux), the vapor quality change will decrease.

The data taken in the present program were taken using both test methods, according to the intended purpose. The incomplete evaporation data reported here (test series no. 1) use the h vs $\dot{m}$ method. Use of this method allows comparison of the present test results with published data. Test series no. 2 was conducted using the Constant Heat Flux Method. The purpose of test series no. 2 was to determine the h vs G plot for the complete evaporation range typical of that used in an evaporator (e.g. from 15% entering vapor quality to a leaving superheat condition).

More detail will be given on each test procedure in the sections that discuss each of these test series.

Data reduction

Details of the data reduction procedure are described by Chamra and Webb [16] and will only be summarized here. Basically, the refrigerant side coefficient was determined by subtracting the water side thermal resistance from the measured overall thermal resistance. The overall heat transfer coefficient (U_o) based on outside area is

$$U_o = \frac{Q_{t,w}}{A_o \Delta T_{lm}}. \quad (1)$$

The log-mean temperature different (ΔT_{lm}) is determined from the annulus-side inlet and outlet tem-

peratures and from the refrigerant saturation temperature.

$$\Delta T_{lm} = \frac{(T_{w,in} - T_{sat}) - (T_{w,out} - T_{sat})}{\ln\left(\frac{(T_{w,in} - T_{sat})}{(T_{w,out} - T_{sat})}\right)}. \quad (2)$$

Assuming no fouling resistance, the refrigerant heat transfer coefficient is determined from

$$h_i = \frac{1}{\left(\frac{1}{U_o} - \frac{1}{h_o} - \frac{D_o \ln(D_o/D_i)}{2k}\right)\frac{A_i}{A_o}}. \quad (3)$$

The refrigerant side coefficient (h_i) is based on the nominal internal surface area $A_i/L = \pi(D_o - 2t_w)$, where D_o is the tube outside diameter and t_w is the wall thickness at the base of the fins (0.50 mm). This definition facilitates direct comparison of different internal geometries having the same outside diameter and wall thickness.

Knowing the calibrated annulus side heat transfer coefficient as a function of water Reynolds number, the tube-side refrigeration coefficient is obtained from equation (3). The heat transfer coefficient (h_i) is based on the nominal (plain tube) inside surface area (A).

The annulus-side heat transfer coefficient correlation is determined experimentally from a water to water Wilson plot technique using measured UA values for a range of water velocities. The annulus-side heat transfer coefficient can be written in the form

$$\frac{h_o D_h}{k} = C\, Re^n\, Pr^{1/3}\left(\frac{\mu}{\mu_w}\right)^{0.14}. \quad (4)$$

The measured $1/UA$ value is the total thermal resistance and is the sum of the inside ($1/h_iA_i$), the wall (R_w) and the annulus-side ($1/h_oA_o$) thermal resistances. Thus

$$\frac{1}{UA} = \frac{1}{h_iA_i} + R_w + \frac{1}{h_oA_o}. \quad (5)$$

Since the inside coefficient (h_i) is held constant, the first and second terms on the right-hand side of equation (5) are constant values for all test points. Substituting equation (4) in equation (5) allows one to write

$$\frac{1}{UA} = C_1 Re^{-n} + C_2 \quad (6)$$

where $C_1 = (CA_o\, Pr^{1/3})^{-1}$ and $C_2 = R_w + 1/(h_iA_i)$, both of which are constants for the test series. Hence, equation (6) is a linear equation, of the form $Y = AX + B$, in which the annulus-side Reynolds number (Re^{-n}) may be interpreted as the variable X. The exponent, n, is determined from the experimental data analysis. The data points are plotted in a Wilson plot where the abscissa is Re^{-n} and the ordinate is $1/UA$. The slope of the "Wilson line" is the value C_1 in equation (6).

Table 2. Experimental uncertainties

Sensors	
Temperature	±0.1°C
Water flow rate	±1.0%
Refrigerant flow rate	±1.0%
Pressure drop	±0.25 kPa
Parameters	
Mass velocity, G [kg m^{-2} s^{-1}]	±2.0%
Vapor quality, x	±4.1%
Heat flux, q'' [W m^{-2}]	±5.4%
Heat transfer coefficient, h [W m^{-2} k^{-1}]	±7.4%

With C_1 known, the constant C in equation (4) can be calculated.

The data points are curve fitted to a straight line, and the curve is extrapolated to $X = 0$ to determine C_2. The Reynolds number exponent (n) was determined from a best-fit regression, which results in the data falling on a straight line.

The uncertainties of the measured and calculated parameters are estimated by following the procedures described by Moffat [17]. The error analysis is done for an average mass flow rate and an average heat flux. The experimental uncertainties associated with the sensors and calculated parameters are listed in Table 2.

TEST SERIES NO. 1

This test series used the "h vs $\dot{m}$ test method," as previously described. Data were taken to span nominal 20% inlet vapor quality and 80% exit vapor quality. For fixed heat flux, the vapor quality over the 2.44 m (8.0 ft) test section length increases. The heat flux increases as the mass flow rate increases in order to maintain 80% exit vapor quality. The higher heat flux is achieved by either increasing the water side flow rate or by increasing the annulus water temperature.

Qualification of test facility

The apparatus was qualified by testing a plain tube for evaporation of R-22. Figure 4(a) shows our test results, and compares them with test results obtained by Thors and Bogart [8] on the same tube geometry. Our tests were performed in an 2.44 m long test section, as compared to the 3.65 m length used by Thors and Bogart [8]. In both cases, the entering and leaving vapor qualities were 20% and 80%, respectively. For the same inlet–exit qualities, the heat flux in the present tests is 33% greater than in those of Thors and Bogart [8]. Chamra and Webb [16] measured the section average evaporation coefficient for constant heat flux. They report that the evaporation coefficient shows a small sensitivity to heat flux for vapor qualities less than 0.5. However, for $x > 0.5$, the heat flux effect is negligible. As shown by Fig. 4(a), the present data tend to fall a little above the Thors and Bogart [8] data.

Figure 4(b) shows a comparison of measured pres-

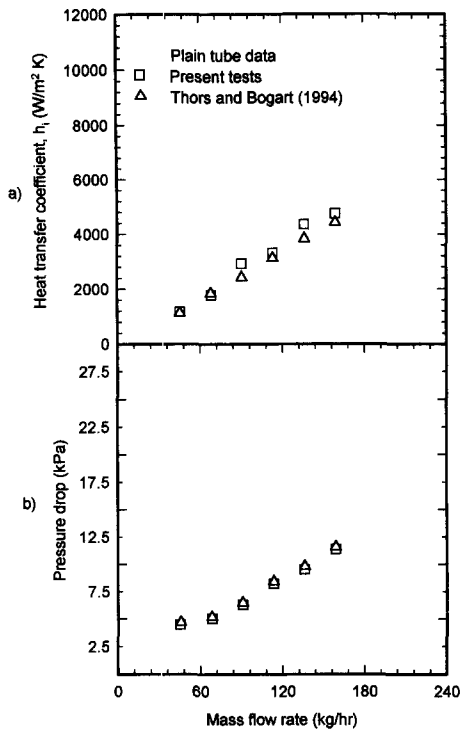

Fig. 4. R-22 data for plain tube: (a) evaporation coefficient; (b) pressure drop.

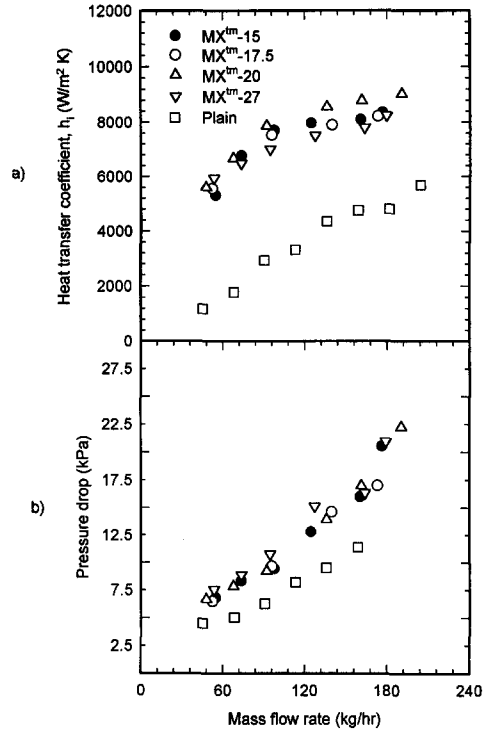

Fig. 5. R-22 evaporation data for four MX^{TM} tubes listed in Table 3 (15, 17.5, 20 and 27° helix angles): (a) evaporation coefficient; (b) pressure drop.

sure drops for the same inlet–exit qualities. As expected, the pressure drop in the 3.65 m long test section of Thors and Bogart [8] is a little higher, because of their 33% longer length. The comparisons shown in Fig. 4 show that our test apparatus provides data in substantial agreement with that obtained by Thors and Bogart [8].

R-22 evaporation data

The heat transfer coefficient and pressure drop test results for the MX^{TM} (single helix) and MCG^{TM} (cross-grooved) tubes are shown in Figs. 5 and 6, respectively. The data for the MX^{TM}-15 tube are shown on each figure for reference purposes.

The results of Figs. 5 and 6 are summarized in numerical format in Table 3. The Table 3 values are based on smooth curve fits of the Figs. 5 and 6 data. This table shows the heat transfer enhancement ratio (h/h_p), the pressure drop ratio ($\Delta p/\Delta p_p$), and the "efficiency index" [$\eta = (h/h_p)/(\Delta p/\Delta p_p)$], where subscript "p" refers to the plain tube. These tabular comparisons are made at 45, 91 and 159 kg h^{-1} mass flow rate. Figures 5 and 6 show that both the evaporation coefficient and the pressure drop increase with increasing flow rate, as expected. However, Table 3 shows that the efficiency index (η) decreases with increasing flow rate.

The "cross-grooved" geometries (MCG^{TM}) are distinctly superior to the MX^{TM}-15 tube, except for the MCG^{TM}-27. The MCG^{TM}-27 performance is lower than the MCG^{TM}-20 tube, because the heat transfer

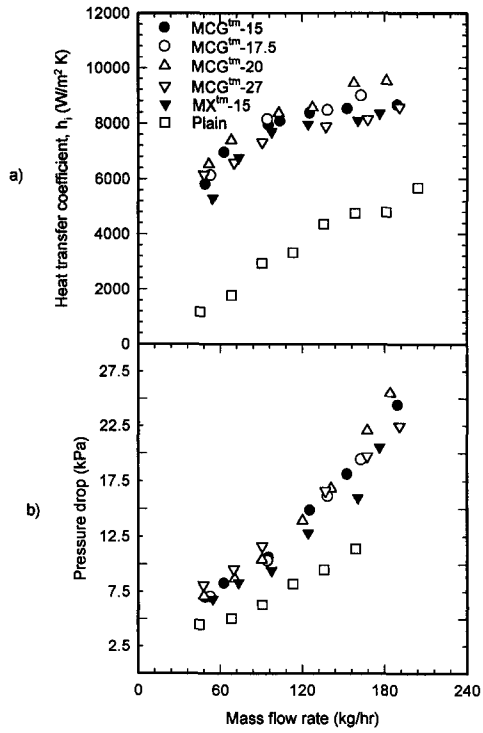

Fig. 6. R-22 evaporation data for four MCG^{TM} tubes listed in Table 3 (15, 17.5, 20 and 27° helix angles): (a) evaporation coefficient; (b) pressure drop.

Table 3. Heat transfer and pressure drop ratios (R-22 evaporation in 2.44 m long test section)

	$\dot{m}$ = 45 kg h^{-1}			$\dot{m}$ = 91 kg h^{-1}			$\dot{m}$ = 159 kg h^{-1}		
	h/h_p	$\Delta p/\Delta p_p$	η	h/h_p	$\Delta p/\Delta p_p$	η	h/h_p	$\Delta p/\Delta p_p$	η
MX™-15	3.56	1.57	2.27	2.74	1.40	1.96	1.82	1.47	1.24
MX™-17.5	3.82	1.52	2.51	2.76	1.40	1.97	1.80	1.39	1.29
MX™-20	4.04	1.54	2.62	2.85	1.42	2.00	1.96	1.48	1.32
MX™-27	4.18	1.60	2.61	2.58	1.64	1.57	1.74	1.52	1.14
DX™-60	2.45	1.38	1.77	2.31	1.41	1.64	1.66	1.47	1.13
DX™-75	2.88	1.41	2.04	2.45	1.42	1.73	1.72	1.59	1.08
MCG™-15 @ 50%	4.27	1.57	2.72	2.90	1.62	1.79	1.92	1.66	1.16
MCG™-17.5 @ 50%	4.23	1.50	2.82	2.95	1.58	1.86	1.95	1.67	1.18
MCG™-20 @ 50%	4.56	1.52	3.00	3.02	1.51	2.00	2.01	1.68	1.20
MCG™-27 @ 50%	4.42	1.78	2.48	2.69	1.82	1.48	1.80	1.64	1.10
MCG™-27 @ 80%	4.21	1.90	2.21	2.55	1.93	1.32	1.70	1.66	1.03

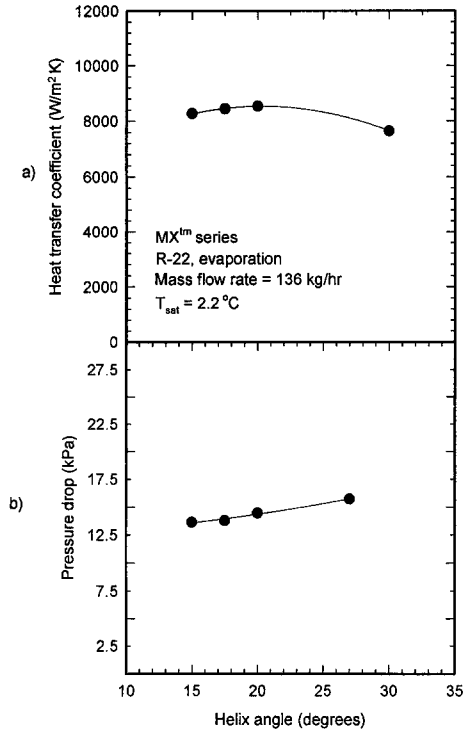

Fig. 7. R-22 evaporation heat transfer coefficient variation with helix angle.

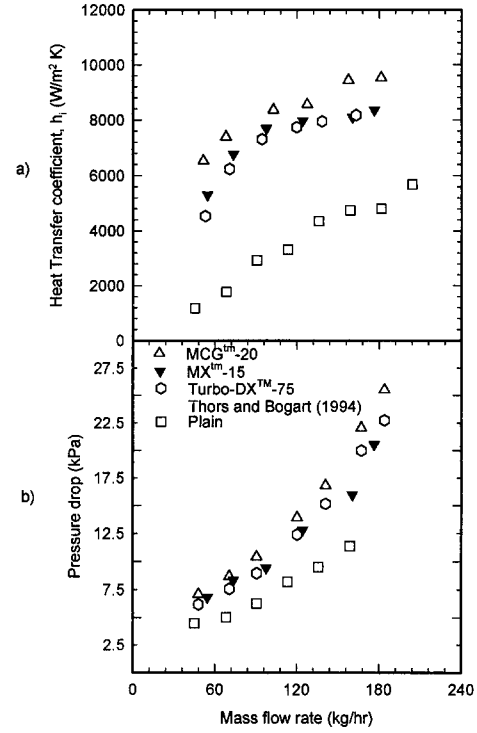

Fig. 8. R-22 evaporation data for MCG™-20 and MX™-15 as compared to Turbo-DX™-75 (Thors and Bogart [8]).

coefficient attains a maximum at 20° and then decreases as the helix angle increases. This is shown in Fig. 7. Ito and Kimura [18] have also shown the existence of an optimum helix angle for single-helix tubes. Table 3 shows that the MCG™-20 tube, at mass flow rate of 91 kg h^{-1}, provides h/h_p = 3.02 vs 2.45 for the DX™-75. Although the pressure drop is 6.3% higher than that of the DX™-75, the heat transfer-to-pressure drop efficiency index (η) is substantially higher (2.00 vs 1.73). The MCG™-20 provides both higher test transfer and same pressure drop as the MX™-20 tube. However, at higher mass flow rate the pressure drop of the MCG™-20 is higher than the MX™-20.

The MX™ tube shows its highest performance at 20° helix angle, as shown in Fig. 5. The same behavior is shown in Fig. 6 for the MCG™ tube performance. Figure 8 shows the heat transfer coefficient and pressure drop for the MCG™-20 and MX™-15, the Turbo-DX™-75 (Thors and Bogart [8]), and plain tubes. At the lower mass flow rates, Table 3 shows that the MX™-15 is superior to the DX™-75 tube (23% higher evaporation coefficient at 45 kg h^{-1}), with the difference narrowing to 5.8% at the highest flow rate. Further, Table 3 shows that the heat transfer/pressure drop ratio is also more favorable for the MX™-15 tube.

Whether the higher heat transfer performance of the MX™-15 and MCG™-20 tubes is useful for application to a refrigerant evaporator requires consideration of both the heat transfer and refrigerant pressure drop. We will address this issue by con-

sidering the tube performance at 91 kg h^{-1}, and take the DX™-75 as the basis for the comparisons to be discussed. The DX™-75 tube provides a 2.45 enhancement factor, relative to the plain tube, and the pressure drop (2.44 m test section) is 1.42 times that of a plain tube. The MX™ series tubes are also single-helix tubes, as is the DX™-75. The best performance of the MX™ series tubes is provided by the 20 degree helix angle. As shown in Table 3, the MX™-20 heat transfer enhancement (h/h_p) is 2.85 vs 2.45 for the DX™-75. Both tubes provide the same pressure drop. Within the MCG™ tubes, the highest enhancement is provided by the MCG™-20 @ 50%. Its heat transfer enhancement ratio is 3.02, and the pressure drop ratio is 1.58 relative to the plain tube. Note that the efficiency index (η) of the MCG™-20 @ 50% is 2.00 as compared to 1.73 for the DX™-75 tube.

Apparently, the higher performance of the MX™-20 tube, relative to the DX™-75 tube, occurs because it has more fins, higher fin height, and lower fin included angle. The performance increase provided by the MCG™ series may be because of the surface area increase.

MCG™ TUBES WITH DIFFERENT SECOND GROOVE DEPTH

The purpose of the tests, using 17.5° helix angle, was to investigate the effect of depth of the second groove for the cross-grooved tube. The different tubes are code named according to the depth of the second groove compared to the height of the first groove. For example, MCG™-17.5 @ 80% denotes that the depth of the second groove is 80% of the first groove height.

Figure 9 shows the evaporation heat transfer coefficient and pressure drop for different second groove depths compared to a plain tube. The second groove depth can provide a small, positive effect on the evaporation performance. The performance increases as the second groove depth is successively increased from 40% to 50% to 60%. Then, the performance falls for the 80% groove depth tube. It is possible that the tips of the microfins become dry for the 80% second depth. The highest performance is provided by the MCG™-17.5 @ 60%, followed by the 50% groove depth. Table 4 shows that the 60% groove depth tube provides 11% higher evaporation coefficient than the MX™-17.5 tube at 91 kg h^{-1} R-22 flow rate. However, the 80% groove depth tube provides only 6% higher evaporation coefficient than the MX™-17.5 tube at 91 kg h^{-1} R-22 flow rate.

Figure 9 also shows the evaporation pressure drop compared to a plain tube. This figure shows that the 50% and 60% groove depths have the highest pressure drop. However, their pressure drop is only a little higher than the 40% and 80% tubes. At 91 kg h^{-1}, the pressure drop of the 60% tube is 8% greater than that of the MX™-17.5 tube. The MCG™-17.5 @ 50% tube has a 3% smaller pressure drop than that of the MCG™-20 tube. The MCG™-17.5 tube has a

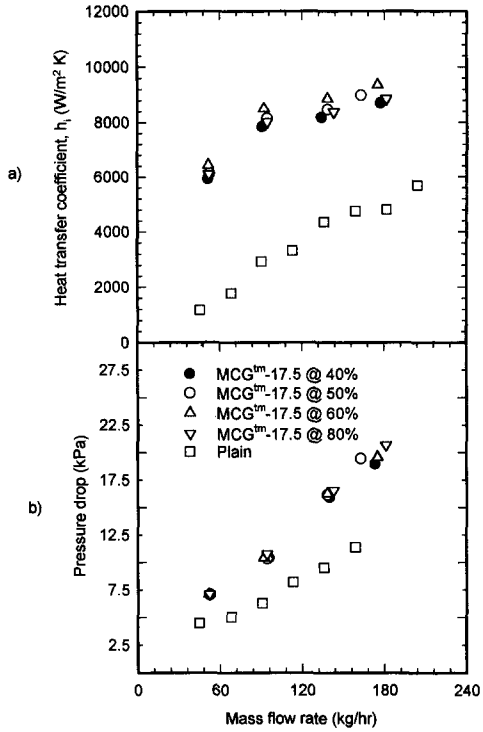

Fig. 9. R-22 evaporation data for four MCG™-17.5 tubes listed in Table 2 with different second groove depth (40%, 50%, 60% and 80%): (a) evaporation coefficient; (b) pressure drop.

lower heat transfer coefficient and a lower pressure drop than that of the MCG™-20 tube. However, the 17.5 at 60% is only 3% lower than the MCG™-20 for a 2% lower pressure drop.

The same results were achieved for the MCG™-27 tubes as shown in Fig. 10. Table 3 and Fig. 10 show that the MCG™-27 at 80% has a lower heat transfer coefficient than the MCG™-27 at 50% for the same pressure drop.

EVAPORATION TEST SERIES NO. 2

This test series used the "constant heat flux" test method, as previously described. The purpose of this test series was to obtain data for the full range of evaporation conditions typically experienced in an evaporator circuit. The refrigerant typically enters at 15–20% vapor quality and leaves at 2–5°C superheat. None of the previously reported investigations on micro-fin tubes have obtained data for exit superheat conditions.

The total circuit length required to attain the exit superheat condition depends on the heat flux. The required circuit length will increase as the heat flux decreases. The data for each Δx-increment in the 2.44 m long test section were taken with constant annulus water inlet temperature. At a given refrigerant flow rate, data were taken for three different nominal values of heat flux. The heat flux establishes the vapor

Table 4. Heat transfer and pressure drop ratios for different second groove depth (R-22 evaporation in 2.44 m long test section)

	$\dot{m}$ = 45 kg h^{-1}			$\dot{m}$ = 91 kg h^{-1}			$\dot{m}$ = 159 kg h^{-1}		
	h/h_p	$\Delta p/\Delta p_p$	η	h/h_p	$\Delta p/\Delta p_p$	η	h/h_p	$\Delta p/\Delta p_p$	η
MCG™-17.5 @ 40%	4.17	1.46	2.85	2.85	1.62	1.76	1.90	1.53	1.24
MCG™-17.5 @ 50%	4.27	1.57	2.72	2.90	1.62	1.79	1.92	1.66	1.16
MCG™-17.5 @ 60%	4.50	1.45	3.10	3.08	1.67	1.84	2.05	1.57	1.31
MCG™-17.5 @ 80%	4.26	1.47	2.90	2.89	1.65	1.75	1.94	1.58	1.23

quality change (Δx) across the test section. The inlet water temperature was adjusted to obtain the desired superheat. The simulated total tubing length required to achieve 2.2°C superheat is the sum of the 2.44 m incremental lengths for $x_{in} = 0.20$ to the exit 2.2°C superheat condition. The three heat flux conditions nominally simulate total circuit lengths of 7.3, 9.75 and 12.2 m. Additional data points were taken to span a range of exit superheat conditions. This was done by reducing the heat flux in the last Δx increment.

This test procedure provided the average heat transfer coefficient (h_{ave}) in the 2.44 m test section vs average vapor quality for simulated circuit lengths of 7.3, 9.75 and 12.2 m. Also obtained was the pressure drop (Δp) in the 2.44 m test section vs average vapor quality in the 2.44 m test section for simulated lengths of 7.3, 9.75 and 12.2 m. The total pressure drop over the full evaporation length (0.20 entering quality to leaving superheat) is obtained by adding the pressure drops for each increment. The abscissa is plotted with two different scales: (1) for the "average vapor quality" abscissa with $x \leqslant 1.0$, the exit vapor quality is less than 1.0 and (2) for the "super heated vapor", abscissa, the exit vapor is superheated (see Table 5 for the leaving superheat condition).

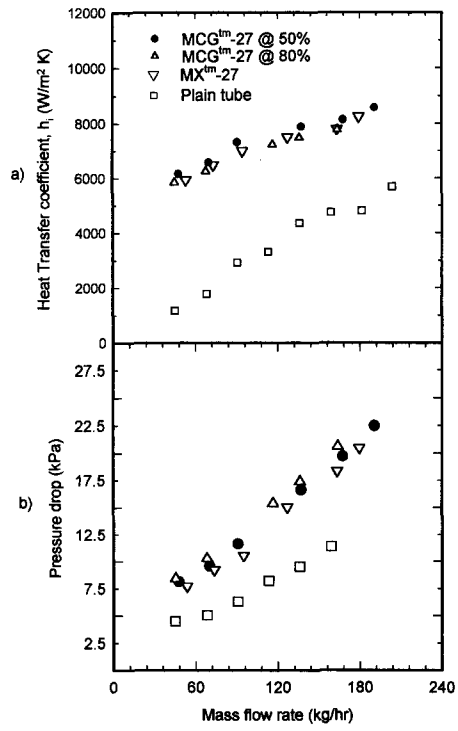

Fig. 10. R-22 evaporation data for MCG™-27 at 50% and 80% tubes: (a) evaporation coefficient; (b) pressure drop.

The test results are shown on Figs. 11(a)–(c) for the R-22 evaporation coefficient in the MCG™-20 tube with inlet $x_{in} \cong 0.15$–0.20 and exit superheat. Figures 11(a)–(c) show the data for 50 kg h^{-1}, 100 kg h^{-1} and 150 kg h^{-1}, respectively. To illustrate the nature of the data, Table 5 provides the data for the plotted points in Fig. 11(b) (100 kg h^{-1}). Table 5 shows the inlet and exit vapor quality, and the heat flux for each of the plotted points. The shapes of Figs. 11(a)–(c) are similar. They show that the sectional average evaporation coefficient attains a maximum at high vapor quality, and then decreases for the exit superheat. The figures show that the vapor quality, at which the maximum evaporation coefficient occurs, decreases for shorter circuit lengths (higher heat flux), and for higher flow rates. For example, the maximum evaporation coefficient occurs at approximately $x = 0.94$ for 50 kg h^{-1} in the 12.2 m circuit, as compared to approximately $x = 0.80$ for 150 kg h^{-1} in the 9.75 m circuit. It appears that the "dry-out" condition is responsible for this phenomenon. At high vapor qualities, the refrigerant is expected to flow as an annular film. At high vapor qualities, the high velocity vapor exerts shear force on the surface of the liquid film, and acts to entrain part of the liquid flow as droplets. Eventually, the wall becomes dry, and the heat transfer coefficient drastically decreases.

Figures 11(a)–(c) show that the sectional average evaporation coefficient decreases with increasing superheat. This is because the heat transfer coefficient to superheated vapor is much less than that for a wetted tube wall. So, the heat flux is reduced for fixed driving temperature difference. This lower performance for exit superheat can have a significant effect on evaporator performance.

APPLICATION CONSIDERATIONS

The MX™-15 and MCG™-20 tubes provide superior heat transfer performance to both the DX™-60 and DX™-75 tubes. By superior, we mean higher evaporation coefficients, and higher values for the heat transfer-to-pressure drop ratio (the efficiency index). However, the pressure drop is also an important factor in design consideration. For fixed compressor suction

Table 5. R-22 Evaporation at 2.2°C in MCG™-20 tube for a flow rate of 150 kg h^{-1}

Pt.	Length [m]	x_{in}	x_{out}	q'' [W m^{-2}]	h [W m^{-2} K^{-1}]	Δp [kPa]
1	12.2	0.22	0.37	7934.0	5144.0	8.30
2	12.2	0.35	0.51	7985.0	6450.0	9.03
3	12.2	0.50	0.66	8076.0	7518.0	10.55
4	12.2	0.66	0.82	8114.0	8329.0	11.45
5	12.2	0.79	0.98	8114.0	8511.0	12.06
6	12.2	0.82	1.8°C superheat	9208.0	6677.0	9.00
1	9.75	0.21	0.44	11984.0	5860.0	8.69
2	9.75	0.43	0.67	12072.0	7574.0	10.41
3	9.75	0.66	0.90	12214.0	8000.0	11.65
4	9.75	0.76	0.22°C superheat	12138.0	7540.0	10.41
5	9.75	0.77	2.3°C superheat	11905.0	5746.0	6.14
1	7.3	0.22	0.53	15528.0	6121.0	9.10
2	7.3	0.50	0.81	15812.0	7864.0	11.38
3	7.3	0.76	0.72°C superheat	12198.0	7239.0	8.76
4	7.3	0.77	2.4°C superheat	11794.0	4701.0	4.76

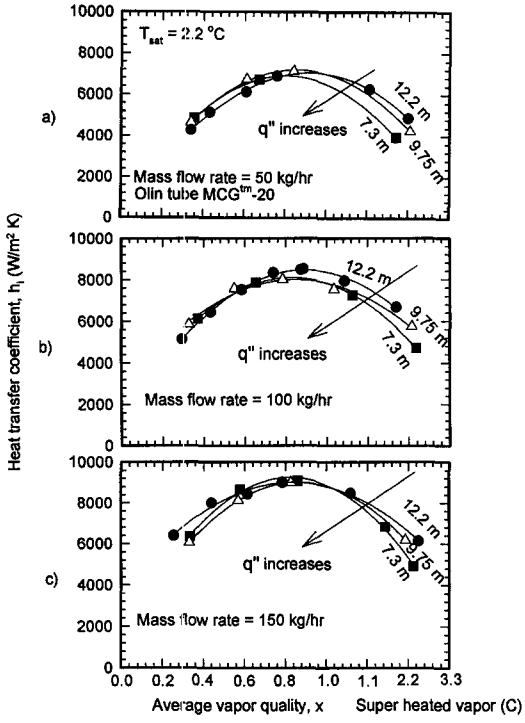

Fig. 11. R-22 evaporation coefficient for MCG™-20 tube with inlet $x_{in} \cong 0.15$–0.20 and exit superheat: (a) 50 kg h^{-1}; (b) 100 kg h^{-1}; (c) 150 kg h^{-1}.

pressure, refrigerant pressure drop will reduce the driving temperature difference. The designer must evaluate the performance of the candidate geometries at the mass flow rate/circuit of interest. Figures 5–7 and Table 3 provide data for flow rates between 45 and 159 kg h^{-1} for this purpose. Whether a given tube geometry is useful depends on whether the designer has freedom of selecting the flow rate/circuit, or whether it is a fixed value.

For consideration of an existing design, one should consider the flow rate/circuit as a fixed value. So, one should be able to use a candidate tube geometry if its heat transfer performance is at least as good as the existing tube and the pressure drop is no higher. Examination of Table 3 shows that at 91 kg h^{-1}, the DX™-75 can replace the DX™-60 tube, because both tubes have the same pressure drop. Table 6 provides an evaluation of whether the MX™-15 and MCG™-20 tubes can replace either the DX™-60 or the DX™-75 tubes for operation at 91 kg h^{-1} per circuit. Table 6 shows that the MX™-15 tube can replace both the DX™-60 or the DX™-75 tubes. Higher heat transfer performance is provided by the MCG™-20 tube. However, its pressure drop is 6.0% higher than of either the DX™-60 or the DX™-75 tubes. A single evaluation is to compare the h-values for operation at equal pressure drop. Analysis by the authors shows that the MCG™-20 tube would provide approximately 14% higher h-value than the DX™-75 tube if operated at a reduced flow rate having the same pressure drop.

Table 6. Comparison of evaporator tube performance at 91 kg h^{-1}

Ratio	MX™-15	MCG™-20
$h/h_{DX™-60}$	1.19	1.31
$\Delta p/\Delta p_{DX™-60}$	0.99	1.06
$\eta/\eta_{DX™-60}$	1.19	1.22
$h/h_{DX™-75}$	1.12	1.23
$\Delta p/\Delta p_{DX™-75}$	0.99	1.06
$\eta/\eta_{DX™-75}$	1.13	1.16

CONCLUSIONS

(1) This work has resulted in the identification of new "micro-grooved" tube geometries that provide higher performance for R-22 evaporation than certain existing commercial products.

(2) At 91 kg h^{-1} evaporation, the MCG™-20 provides 31% and 23% higher evaporation coefficient than the DX™-60 and DX™-75 tubes respectively. The associated pressure drop penalty is 6%. The single-groove MX™-15 tube provides 19% and 12% higher evaporation coefficient than the DX™-60 and DX™-75 tubes, respectively. The pressure drops are equal.

(3) The maximum evaporation coefficient occurs at 20° helix angle for all the micro-fin tubes. For the MCG™ series, the depth of the second groove has a marginal effect on the heat transfer. The evaporation heat transfer coefficient reaches a maximum at 60% second groove depth. The cross-grooving leads to a higher pressure drop. However, the pressure drop is almost the same for different second groove depths.

(4) Data are also reported to define the evaporation coefficient at high vapor quality, which extends into the superheat region. The data show that the heat transfer coefficient of the MCG™-20 tube is substantially superior to the plain tube, not only in the vapor quality region, but also after the dry-out condition has been attained.

(5) Apparently, the higher performance of the current MX™ and MCG™ tubes occurs because these tubes have more fins, higher fin height, and lower fin included angle.

Acknowledgements—The authors would like to express their thanks to Olin Brass for supporting this project and providing the tubes. We would also like to acknowledge that Wolverine Tube Inc. donated the apparatus on which the data were taken.

REFERENCES

1. R. L. Webb, *Principles of Enhanced Heat Transfer*. Wiley Interscience, New York (1994).
2. K. Fujie, N. Itoh, T. Innami, H. Kimura, N. Nakayama and T. Yanugidi, Heat transfer pipe. U.S. Patent 4 044 797, assigned to Hitachi Ltd (1977).
3. A. Tatsumi, K. Oizumi, M. Hayashi and M. Ito, Application of inner groove tubes to air conditioners, *Hitachi Rev.* **32**(1), 55–60 (1982).
4. Y. Shinohara and M. Tobe, Development of an improved thermofin tube, *Hitachi Cable Rev.* **4**, 47–50 (1985).
5. Y. Shinohara, K. Oizumi, Y. Itoh and M. Hori, Heat transfer tubes with grooved inner surface. U.S. Patent 4 658 892, assigned to Hitachi Cable Ltd (1987).
6. S. J. Eckels, M. B. Pate and C. H. Bemisderfer, Evaporation heat transfer coefficients for R-22 in micro-fin tubes of different configurations. In *Enhanced Heat Transfer* (Edited by M. B. Pate and M. K. Jensen), ASME Symposium Volume, HTD-Vol. 202, pp. 117–126. ASME, New York (1992).
7. L. M. Schlager, M. B. Pate and A. E. Bergles, Evaporation and condensation heat transfer and pressure drop in horizontal, 12.7-mm micro-fin tubes with refrigerant, 22, *J. Heat Transfer* **112**, 1041–1047 (1990).
8. P. Thors and J. E. Bogart, In-tube evaporation of HCFC-22 with enhanced tubes, *J. Enhanced Heat Transfer* **1**(4), 365–377 (1994).
9. H. Morita, Y. Kito and Y. Satoh, Recent improvements in small bore inner grooved copper tube, *Tube Pipe Technol.* 53–57 November/December (1993).
10. R. Chiang, Heat transfer and pressure drop during evaporation and condensation of refrigerant-22 in 7.5 mm diameter axial and helical grooved tubes, *A.I.Ch.E. Symp. Ser.* 295, **89**, 205–210 (1993).
11. L. M. Schlager, M. B. Pate and A. E. Bergles, Performance of micro-fin tubes with refrigerant-22 and oil mixtures. *ASHRAE J.* **94**(1), 17–28 (1988).
12. L. M. Schlager, A. E. Bergles and M. B. Pate, Evaporation and condensation of refrigerant–oil mixtures in a smooth tube and a micro-fin tube, *ASHRAE Trans.* **94**(1), 149–166 (1988).
13. S. J. Eckels and M. B. Pate, In-tube evaporation and condensation of refrigerant–lubricant mixtures of HFC-134a and CFC-12, *ASHRAE Trans.* **97**(2), 62–70 (1991).
14. S. Ha and A. E. Bergles, Some aspects of experimental in-tube evaporation, *Heat Transfer* 1994, *Proc. Tenth International Heat Transfer Conference*, Vol. 6, pp. 187–192 (1994).
15. S. Yoshida, T. Matsunaga and H. P. Hong, Heat transfer to refrigerants in horizontal evaporator tubes with internal, spiral grooves, *Proceedings* 1987 *ASME–JSME Thermal Engineering Joint Conference* (Edited by P. J. Marto), Vol. 5, pp. 165–172 (1987).
16. L. M. Chamra and R. L. Webb, Condensation and evaporation in micro-fin tubes at equal saturation temperatures, *J. Enhanced Heat Transfer* **2**(3), 219–229 (1995).
17. Robert J. Moffat, Describing the uncertainties in experimental results, *Exp. Thermal Fluid Sci.* **1**, 3–17 (1988).
18. M. Ito and H. Kimura, Boiling heat transfer and pressure drop in internal spiral-grooved tubes, *Bull. JSME* **22**(17), 1251–1257 (1979).